


## Scanning Tunneling Thermometry

Abhay Shastry<sup>1,2,\*</sup>, Sosuke Inui<sup>1,3</sup> and Charles A. Stafford<sup>1</sup>

<sup>1</sup>*Department of Physics, University of Arizona, Tucson, Arizona 85721, USA*

<sup>2</sup>*Chemical Physics Theory Group, Department of Chemistry, University of Toronto, 80 St. George Street, Toronto, Ontario M5S 3H4, Canada*

<sup>3</sup>*Department of Physics, Osaka City University, Sugimoto 3-3-138, Sumiyoshi-Ku, Osaka 558-8585, Japan*

 (Received 4 June 2019; revised manuscript received 18 November 2019; accepted 2 January 2020; published 25 February 2020)

The best spatial resolution so far achieved in thermal imaging is several nanometers, much coarser than routinely achieved for other physical properties. Here we propose a method to map electronic temperature variations in operating nanoscale conductors by relying solely upon electrical tunneling current measurements. The proposed measurement scheme involves two scanning probe operations to measure the conductance and thermopower, respectively. These two measurements are shown to determine the local temperature with high accuracy in nanoscale conductors, where the Wiedemann-Franz law holds quite generally. The proposed scanning tunneling thermometer, owing to its operation in the tunneling regime, would be capable of mapping temperature variations with subnanometer resolution, thereby enhancing the resolution of scanning thermometry by some 2 orders of magnitude.

DOI: [10.1103/PhysRevApplied.13.024065](https://doi.org/10.1103/PhysRevApplied.13.024065)

### I. INTRODUCTION

Thermal imaging of nanoscale systems is of crucial importance not only due to its potential to enable future technologies, but also because it can greatly enhance our understanding of heat transport at the smallest scales. In recent years, nanoscale thermometry has been used in a wide range of fields [1], including thermometry in a living cell [2], local control of chemical reactions [3], and temperature mapping of operating electronic devices [4]. Various studies utilize radiation-based techniques such as Raman spectroscopy [5], fluorescence in nanodiamonds [2,6], and near-field optical microscopy [7]. The spatial resolution of these radiation-based techniques is limited due to optical diffraction and, to overcome this drawback, scanning-probe techniques have seen a flurry of activity in recent years [8]. However, despite their remarkable progress, the spatial resolution remains in the 10-nm range. A key obstacle to achieving high spatial resolution in scanning-probe thermometry has been the fundamental difficulty in designing a thermal probe that exchanges heat with the system of interest but is thermally isolated from the environment.

Since temperature and voltage are both fundamental thermodynamic observables, it is instructive to draw the sharp contrast that exists between the measurement of these two quantities at the nanoscale. Scanning tunneling potentiometry (STP) [9] is a mature technology and can

map local voltage variations with subangstrom spatial resolution by operating in the tunneling regime. STP has been used to map the local voltage variations in the vicinity of individual scatterers, interfaces, or boundaries [10–14], providing direct observations of the Landauer dipole [15,16]. STP has been a useful tool in disentangling different scattering mechanisms [14] and can map local potential variations due to quantum interference effects [12,13]. Similarly, local temperature variations due to quantum interference effects have been theoretically predicted for various nanosystems out of equilibrium [17–20] but have hitherto remained outside the reach of experiment.

Scanning thermal microscopy [21] (SThM) relies on the measurement of a heat-flux signal that can be sensed, e.g., by a calibrated thermocouple or an electrical resistor [22]. A good thermal contact between the tip and sample is needed for an appreciable heat flux and generally implies a measurement in the contact regime, thus limiting the spatial resolution. Despite the recent progress in addressing contact-related issues in SThM [8,23], the best spatial resolution is presently approximately 7 nm [24].

It is well known that, outside equilibrium, the temperatures of different degrees of freedom (e.g., phonon, photon, electron) do not coincide [25]; existing SThM schemes cannot distinguish between the contributions of the different degrees of freedom to the heat flux. A number of nanoscopic devices operate in the elastic transport regime where the electron and phonon degrees of freedom are completely decoupled and, consequently, the distinction between their temperatures becomes extremely important [26].

\*abhayshastry@email.arizona.edu

From a fundamental point of view, a thermometer is a device that equilibrates locally with the system of interest and has some temperature-dependent physical property (e.g., resistance, thermopower, mass density), which can be measured; the temperature measurement seeks to find the condition(s) under which the thermometer is in local thermodynamic equilibrium with the system of interest and concurrently infers the thermometer's temperature by relying upon those temperature-dependent physical properties. Ideally, the measurement apparatus must not substantially disturb the state of the system of interest [27]. SThM schemes, by relying on heat fluxes in the contact regime, may alter the state of a small system.

We propose here a noninvasive thermometer whose local equilibration can be inferred by the measurement of electrical tunneling currents alone. Ours is a theoretical proposal only but we detail fully how the experiment may be performed. In particular, we find that the conditions required for the local equilibration of the *scanning tunneling thermometer* (STTh) are completely determined by (a) the conductance and thermopower, which are both measured using the tunneling current and (b) the bias conditions of the conductor defined by the voltages and temperatures of the contacts. The validity of our proposed measurement scheme is demonstrated with simulations of the temperature distribution in a model nanoscale conductor (graphene nanoflake) under various thermoelectric bias conditions. Many additional details, including importantly those pertaining to the resolution of the tunneling currents, are given in the appendixes.

Our proposed method relies solely upon electrical measurements made in the tunneling regime and provides a measurement of the *electronic* temperature decoupled from all other degrees of freedom. We predict a dramatic enhancement of the spatial resolution by more than 2 orders of magnitude, thereby bringing thermometry to the subangstrom regime. The method is valid for systems obeying the Wiedemann-Franz (WF) law [28], which relates the electrical ( $G$ ) and thermal conductances ( $\kappa$ ) in a material-independent way  $\kappa/G = \pi^2 k_B^2 T/3e^2$ . The WF law was first observed in bulk metals over 150 years ago and has been verified in a large number of nanoscale conductors. Most recently, it has been validated in atomic contact junctions [29,30], which represent the ultimate limit of miniturization of electronic conductors.

## II. TEMPERATURE MEASUREMENT

We note a crucial, but often overlooked, theoretical point pertaining to the imaging of temperature fields on a nonequilibrium conductor. The prevailing paradigm for temperature and voltage measurements is the following [31]: (i) a voltage is measured by a probe (voltmeter) when in electrical equilibrium with the sample and (ii) a temperature is measured by a probe (thermometer) when in thermal

equilibrium with the sample. We refer to this definition as the Engquist-Anderson (EA) definition.

The fact that the EA definition implicitly ignores thermoelectric effects was pointed out by Bergfeld and Stafford [18,32], and a notion of a joint probe was put forth by requiring *both* electrical and thermal equilibrium with the sample. It is quite easy to understand this intuitively: a temperature probe lacking local electrical equilibration with the sample develops a temperature bias at the probe-sample junction due to the Peltier effect; similarly, a voltage probe lacking local thermal equilibration with the sample develops a voltage bias at the probe-sample junction due to the Seebeck effect. These errors [32] can be quite large for systems with large thermoelectric responses. A temperature probe therefore has to remain in thermal *and* electrical equilibrium with the nonequilibrium sample [18,19,26,27,32,33], thereby ensuring true *thermodynamic* equilibrium of the measurement apparatus.

The joint probe measurement was made mathematically rigorous in a recent study by Shastry and Stafford [27] where it was shown that the solution to the probe equilibration problem always exists and is unique, arbitrarily far from equilibrium and with arbitrary interactions within the quantum system. Moreover, it was shown that the EA definition is provably nonunique: the value measured by the EA thermometer depends quite strongly on its voltage and, conversely, the value measured by the EA voltmeter depends on its temperature. These results are intimately connected to the second law of thermodynamics and expose the fatal flaw in the EA definition: the measurement apparatus (thermometer or voltmeter) has to remain in *thermodynamic* equilibrium, i.e., *electrical* and *thermal* equilibrium, with the system of interest which it probes locally. Simply stated, an open system of electrons (a conductor) exchanges both charge *and* heat. We therefore write

$$I_p = 0; \quad J_p = 0, \quad (1)$$

for the simultaneous vanishing of the electric current  $I_p$  and the *electronic* contribution to the heat current  $J_p$  flowing into the probe  $p$ . The above equation determines the conditions under which a local thermodynamic equilibrium is established between the probe (STTh) and the nonequilibrium system of interest.

## III. TEMPERATURE FROM TUNNELING CURRENTS

The probe currents depend linearly on the temperature and voltage gradients for transport within the linear response regime:

$$\begin{pmatrix} I_p \\ J_p \end{pmatrix} = \sum_{\alpha} \begin{pmatrix} \mathcal{L}_{p\alpha}^{(0)} & \mathcal{L}_{p\alpha}^{(1)} \\ \mathcal{L}_{p\alpha}^{(1)} & \mathcal{L}_{p\alpha}^{(2)} \end{pmatrix} \begin{pmatrix} V_{\alpha} - V_p \\ \frac{T_{\alpha} - T_p}{T_0} \end{pmatrix}, \quad (2)$$

where the  $\mathcal{L}_{p\alpha}^{(v)}$  are the Onsager linear response coefficients evaluated at the equilibrium temperature  $T_0$  and chemical potential  $\mu_0$ .  $\mathcal{L}_{p\alpha}^{(0)}$  is the electrical conductance [ $\mathcal{L}_{p\alpha}^{(0)} = G_{p\alpha}$ ] between the probe  $p$  and contact  $\alpha$ .  $\mathcal{L}_{p\alpha}^{(1)}$  is related to the thermopower ( $S_{p\alpha}$ ) and electrical conductance [ $\mathcal{L}_{p\alpha}^{(1)} = -T_0 S_{p\alpha} G_{p\alpha}$ ]. Finally,  $\mathcal{L}_{p\alpha}^{(2)}$  is related to the thermal conductance [ $\mathcal{L}_{p\alpha}^{(2)} = T_0 \kappa_{p\alpha}$ ] up to leading order in the Sommerfeld series [28] (see also Appendix C).

We solve for the temperature of the STTh in Eq. (1) and find [19]

$$\begin{aligned} \frac{T_p^{(\text{exact})}}{T_0} &= \frac{\sum_{\beta} \mathcal{L}_{p\beta}^{(0)} \sum_{\alpha} \mathcal{L}_{p\alpha}^{(1)} V_{\alpha} - \sum_{\beta} \mathcal{L}_{p\beta}^{(1)} \sum_{\alpha} \mathcal{L}_{p\alpha}^{(0)} V_{\alpha}}{\sum_{\beta} \mathcal{L}_{p\beta}^{(2)} \sum_{\alpha} \mathcal{L}_{p\alpha}^{(0)} - [\sum_{\alpha} \mathcal{L}_{p\alpha}^{(1)}]^2} \\ &+ \frac{1}{T_0} \frac{\sum_{\beta} \mathcal{L}_{p\beta}^{(0)} \sum_{\alpha} \mathcal{L}_{p\alpha}^{(2)} T_{\alpha} - \sum_{\beta} \mathcal{L}_{p\beta}^{(1)} \sum_{\alpha} \mathcal{L}_{p\alpha}^{(1)} T_{\alpha}}{\sum_{\beta} \mathcal{L}_{p\beta}^{(2)} \sum_{\alpha} \mathcal{L}_{p\alpha}^{(0)} - [\sum_{\alpha} \mathcal{L}_{p\alpha}^{(1)}]^2}. \end{aligned} \quad (3)$$

Here  $T_p^{(\text{exact})}$  denotes the exact solution to the equilibration of the STTh, i.e., Eq. (1), within the linear response regime where the currents are expressed by Eq. (2).

Equation (2) suggests that  $\mathcal{L}_{p\alpha}^{(0)}$  and  $\mathcal{L}_{p\alpha}^{(1)}$  can be measured using the tunneling current  $I_p$ , whereas  $\mathcal{L}_{p\alpha}^{(2)}$  appears only in the expression for the heat current  $J_p$  and would generally involve the measurement of a heat-flux-related signal. However, for systems obeying the WF law, we may simply relate  $\mathcal{L}_{p\alpha}^{(0)}$  and  $\mathcal{L}_{p\alpha}^{(2)}$  using

$$\mathcal{L}_{p\alpha}^{(2)} = \frac{\pi^2 k_B^2 T_0^2}{3e^2} \mathcal{L}_{p\alpha}^{(0)} \left[ 1 + \mathcal{O} \left( \frac{k_B T_0}{\Delta} \right)^2 + \dots \right], \quad (4)$$

where the characteristic energy scale of the problem  $\Delta$  is typically much larger than the thermal energy set by  $k_B T_0$ : e.g.,  $\Delta = \epsilon_F$ , the Fermi energy, for bulk systems and for a tunneling probe  $\Delta$  is of the order of the work function. The Wiedemann-Franz law arises whenever the transport is dominated by elastic scattering processes as shown explicitly in Appendix C. It is valid in most normal metals since the electron-phonon scattering is quasielastic at room temperatures ( $k_B T \ll \epsilon_F$ ). The breakdown of the Wiedemann-Franz law has been reported in various nanoscale systems. The characteristic energy scale  $\Delta$  in such cases is comparable to the thermal energy thereby leading to large corrections from the higher-order terms in the series expansion, Eq. (6). In graphene, the breakdown of the WF law was reported in Ref. [34]. Here, the local chemical potential was tuned (via local doping) such that it is smaller than the thermal energy thereby creating the so-called Dirac fluid. Such systems show a decoupling of charge and heat currents, making it impossible to measure heat currents through electrical means. Although our results apply to a broad array of nanoscale conductors, they do not apply to systems prepared in this manner.

Using the WF law given by Eq. (4) to infer  $\mathcal{L}_{p\alpha}^{(2)}$ , we obtain

$$\begin{aligned} \frac{T_p^{(\text{WF})}}{T_0} &= \frac{3e^2}{\pi^2 k_B^2 T_0^2} \left[ \frac{\sum_{\alpha} \mathcal{L}_{p\alpha}^{(1)} V_{\alpha}}{\sum_{\alpha} \mathcal{L}_{p\alpha}^{(0)}} - \frac{\sum_{\alpha} \mathcal{L}_{p\alpha}^{(1)} \sum_{\beta} \mathcal{L}_{p\beta}^{(0)} V_{\beta}}{\sum_{\alpha} \mathcal{L}_{p\alpha}^{(0)} \sum_{\beta} \mathcal{L}_{p\beta}^{(0)}} \right] \\ &+ \frac{\sum_{\alpha} \mathcal{L}_{p\alpha}^{(0)} T_{\alpha}}{T_0 \sum_{\alpha} \mathcal{L}_{p\alpha}^{(0)}}, \end{aligned} \quad (5)$$

valid up to leading order in the Sommerfeld series.  $T_p^{(\text{WF})}$  requires only the measurement of  $\mathcal{L}_{p\alpha}^{(0)}$  and  $\mathcal{L}_{p\alpha}^{(1)}$ , or equivalently, the electrical conductance and thermopower, and lends itself to a simple interpretation: The first term in Eq. (5) is the thermoelectric contribution whereas the second term is the thermal contribution. The second-order corrections (see Appendix C for more details) in the Sommerfeld series are typically very small

$$T_p^{(\text{WF})} = T_p^{(\text{exact})} \left[ 1 + \mathcal{O} \left( \frac{k_B T_0}{\Delta} \right)^2 + \dots \right]. \quad (6)$$

It is clear from Eq. (5) that the measurement of (a) conductance  $\mathcal{L}_{p\alpha}^{(0)}$  and the thermoelectric coefficient  $\mathcal{L}_{p\alpha}^{(1)}$  along with the (b) known bias conditions of the system  $\{V_{\alpha}, T_{\alpha}\}$  completely determine the conditions under which the STTh is in local thermodynamic equilibrium with the system.

#### IV. PROPOSED EXPERIMENTAL IMPLEMENTATION

The temperature measurement involves two circuits: (I) the conductance circuit, which measures the electrical conductance  $\mathcal{L}_{p\alpha}^{(0)}$  and (II) the thermoelectric circuit, which measures the thermoelectric response coefficient  $\mathcal{L}_{p\alpha}^{(1)}$ , as shown in Figs. 1(b) and 1(c), respectively. The STTh involves operating the tip of a scanning tunneling microscope (STM) at a constant height above the surface of the conductor in the tunneling regime. The circuit operations (I) and (II) are described below.

(I) *The conductance circuit* involves a closed circuit of the probe and the contact  $\alpha$ . All contacts and the probe are held at the equilibrium temperature  $T_{\alpha} = T_p = T_0$ . An ac voltage  $V(\omega)$  is applied at the probe-contact junction  $V(\omega) = V_p - V_{\alpha}$  and the resulting tunneling current  $I_p(\omega)$  is recorded using standard lock-in techniques. The STM tip is scanned along the surface. A switch disconnects all contacts except  $\alpha$  and the tunneling current is therefore

$$\begin{aligned} I_p &= \mathcal{L}_{p\alpha}^{(0)} (V_p - V_{\alpha}) = -I_{\alpha}, \\ I_p(\omega) &= \mathcal{L}_{p\alpha}^{(0)} V(\omega). \end{aligned} \quad (7)$$

The procedure is repeated for all the contacts  $\alpha$  by toggling the switch  $S$  shown in Fig. 1(b) and a scan is obtained for

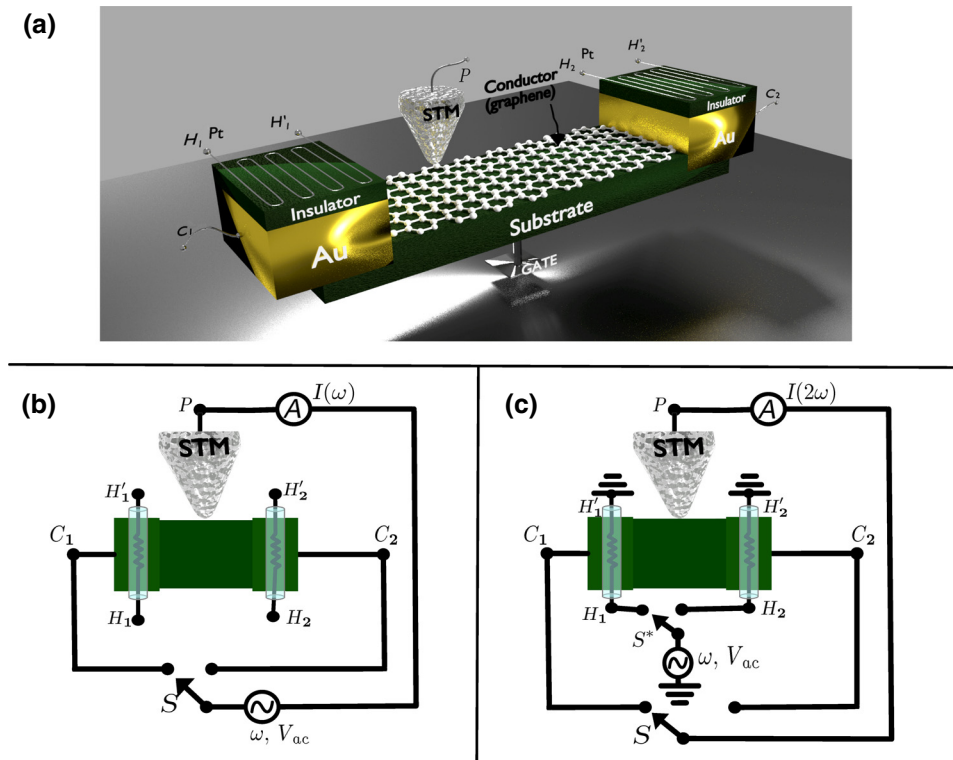


FIG. 1. (a) Schematic depiction of the system and measurement apparatus. An STM tip scans the surface of a nanoscale conductor at a fixed height. The conductor sits on top of a substrate which may be gated. Two gold contacts  $C_1$  and  $C_2$  are connected to the conductor on either side. A Pt heater ( $H_1H_1'$  and  $H_2H_2'$ ) sitting atop each gold contact, and electrically insulated from it, allows one to modulate the temperature of the gold contacts. (b) The conductance circuit, which measures the coefficient  $\mathcal{L}_{p\alpha}^{(0)}$  for each contact  $\alpha$  selected using switch  $S$ . (c) The thermoelectric circuit, which measures the coefficient  $\mathcal{L}_{p\alpha}^{(1)}$  for each contact  $\alpha$ . Switch  $S^*$  activates the heater in the corresponding contact  $\alpha$  selected by switch  $S$ .

each probe-contact junction. This completes the measurement of the conductance  $\mathcal{L}_{p\alpha}^{(0)}$  for all the contacts  $\alpha$ .

(II) *The thermoelectric circuit* involves a (i) closed circuit of the probe and contact  $\alpha$ , which is the same as the conductance circuit without the voltage source, and (ii) an additional circuit, which induces time-modulated temperature variations in contact  $\alpha$ ; an ac current at frequency  $\omega$  induces Joule heating in the Pt resistor at frequency  $2\omega$  and results in a temperature modulation  $T_\alpha = T_0 + \Delta T_\alpha(2\omega)$  in the contact  $\alpha$ . The probe is held at the equilibrium temperature  $T_p = T_0$ . The resulting tunneling current  $I_p(2\omega)$ , at frequency  $2\omega$ , is recorded using standard lock-in techniques. The STM tip is scanned along the surface at the same points as before. A switch disconnects all contacts except  $\alpha$  and the tunneling current is

$$I_p = \mathcal{L}_{p\alpha}^{(1)} \frac{(T_\alpha - T_p)}{T_0} = -I_\alpha, \quad (8)$$

$$I_p(2\omega) = \mathcal{L}_{p\alpha}^{(1)} \frac{\Delta T_\alpha(2\omega)}{T_0}.$$

The procedure is repeated for all the contacts  $\alpha$  by toggling the switches  $S$  and  $S^*$  shown in Fig. 1(c) and a scan is obtained for each probe-contact junction. Note that the switch  $S^*$  must heat the Pt resistor in the same contact  $\alpha$  for which the probe-contact tunneling current is measured. This completes the measurement of the thermoelectric coefficient  $\mathcal{L}_{p\alpha}^{(1)}$  for all the contacts  $\alpha$ .

Heating elements have been fabricated in the contacts previously [35]. Any system where one may induce Joule

heating can be used as the heating element (instead of Pt) in the circuit. For example, another flake of graphene could be used as a heating element as long as it is calibrated accurately. The voltage modulation frequency in the heating elements  $\omega \ll 1/\tau$ , where  $\tau$  is the thermal time constant of the contacts, so that the contact may thermalize with the heating element. Typically,  $\tau$  is of the order of tens of nanoseconds (cf. methods in [18]). We discuss the calibration of the contact temperature  $T_\alpha = T_0 + \Delta T_\alpha$  in Appendix D. The thermoelectric response of the nanosystem may be quite sensitive to the gate voltage, which is also discussed in Appendix E 1 a.

## V. NUMERICAL RESULTS AND DISCUSSION

We present model temperature measurements for a hexagonal graphene flake under (a) a thermal bias and (b) a voltage bias. The measured temperature, for a combination of thermal and voltage biases, would simply be a linear combination of the two scenarios (a) and (b) in the linear response regime (under identical gating conditions). Therefore, we present the two cases separately but we note that the gate voltages are not the same for the two scenarios that we present here. The voltage bias case has been gated differently so as to enhance the thermoelectric response of the system (see Appendix E 1 a for a more detailed discussion). We show the temperature measurement for (a) the thermal bias case in Fig. 2 and (b) the voltage bias case in Fig. 3. The two panels in Figs. 2 and 3 compare (1) the temperature measurement  $T_p^{(\text{exact})}$  obtained from the exact



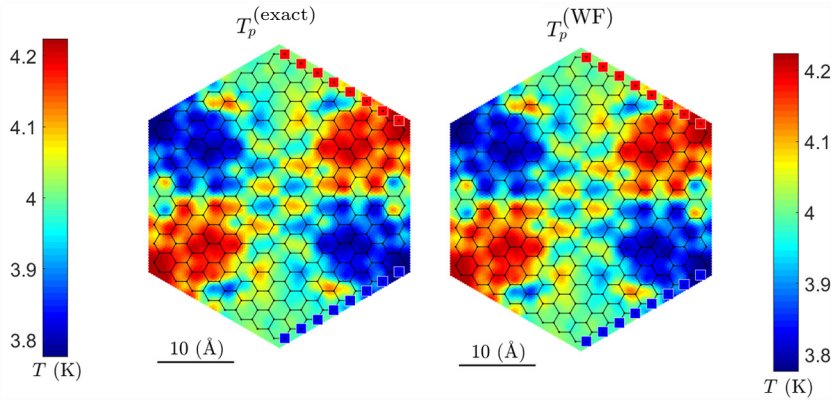


FIG. 2. Temperature variations on a hexagonal graphene flake with an application of a symmetrical temperature bias  $T_{\text{red}} - T_{\text{blue}} = 0.5$  K, where the red (hot) and blue (cold) squares indicate the sites coupled to the contacts;  $T_0 = 4$  K. The left panel shows the exact linear response solution given in Eq. (3) while the right panel shows the WF solution given by Eq. (5). The same temperature scale is used for both panels. The STTh tip is scanned at a constant height of  $3 \text{ \AA}$  above the plane of the graphene flake.

solution [given by Eq. (3)] and (2) the temperature measurement  $T_p^{(\text{WF})}$  obtained from our method [given by Eq. (5)], which relies on the WF law.

Graphene is highly relevant for future electronic technologies and provides a versatile system whose transport properties can be tuned by an appropriate choice of the gate voltage—we therefore illustrate our results for graphene. The method itself is valid for any system obeying the WF law. The thermoelectric response coefficient  $\mathcal{L}_{p\alpha}^{(1)} \sim T_0^2$  has a quadratic suppression at low temperatures and its measurement from Eq. (8) depends crucially on the choice of gating especially at cryogenic operating temperatures since the resulting tunneling current must be experimentally resolvable. In graphene, we find that the electrical tunneling currents arising from its thermoelectric response are resolvable even at cryogenic temperatures when the system is gated appropriately and, owing to the fact that a number of STM experiments are conducted at low temperatures, we present our results for  $T_0 = 4$  K. Higher operating temperatures result in a higher tunneling current in Eq. (8) and gating would therefore be less important.

The  $\pi$ -electron system of graphene is described using the tight-binding model whose basis states are  $2p_z$  orbitals at each atomic site of carbon. The STTh is modeled as an atomically sharp Pt tip operating at a constant height of  $3 \text{ \AA}$  above the plane of the carbon nuclei. The details of the

graphene Hamiltonian as well as the probe-system tunnel coupling are presented in Appendixes A and B, respectively. The atomic sites of graphene which are coupled to the contacts are indicated in Figs. 2 and 3 by either a red or blue square. The chemical potential and temperature of the two contacts (red and blue) set the bias conditions for the problem. The coupling to the two contacts is symmetrical and the coupling strength for all the coupling sites (red or blue) is taken as  $\Gamma = 0.5$  eV. Additional details regarding the gating and the tunneling currents are included in Appendix D.

Figure 2 shows the variations in temperature for a symmetrical ( $T_{\text{red}} + T_{\text{blue}} = 2T_0$ ) temperature bias  $T_{\text{red}} - T_{\text{blue}} = 0.5$  K. The agreement between  $T_p^{(\text{exact})}$  and  $T_p^{(\text{WF})}$  given by Eqs. (3) and (5), respectively, is excellent. The gating has been chosen to be  $\mu_0 = -2.28$  eV with respect to the Dirac point in graphene. The same temperature scale is used for both the panels in Fig. 2. The temperature variations in  $T_p^{(\text{WF})}$  are solely the result of the temperature bias and are given by the second term in Eq. (5). Therefore, we require only the measurement of the conductances  $\mathcal{L}_{p\alpha}^{(0)}$  for the temperature measurement under these bias conditions. We consider a contact-tip voltage modulation of 1 mV for the measurement of the conductance. The resulting tunneling currents are of the order of 10 nA with a maximum tunneling current of about 30 nA. We present the details in Appendix E.

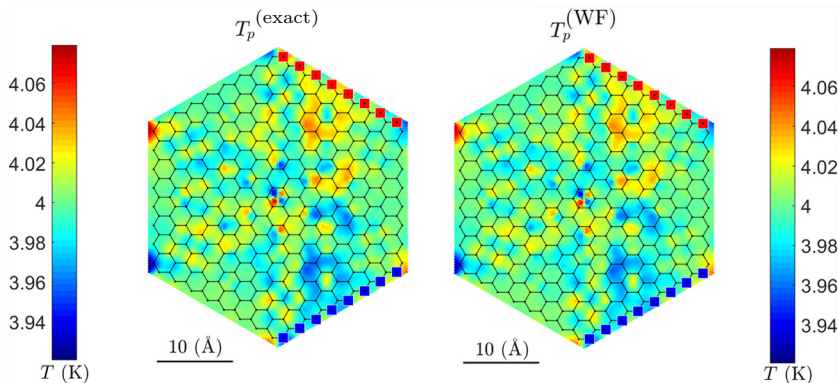


FIG. 3. Temperature variations on a hexagonal graphene flake with an application of a voltage bias  $V_{\text{blue}} - V_{\text{red}} = k_B T_0 / e = 0.34$  mV, where the red and blue squares indicate the sites coupled to the contacts;  $T_0 = 4$  K. The left panel shows the exact linear response solution given in Eq. (3) while the right panel shows the approximate solution obtained by employing the WF law given in Eq. (5). The same temperature scale is used for both panels. The STTh tip is scanned at a constant height of  $3 \text{ \AA}$  above the plane of the graphene flake.

The model system considered in this section represents a quantum coherent conductor with no inelastic scattering within the system which may lead to a “mixing” of the electron waves emanating from the two reservoirs. The local temperature, however, is well-defined [Eq. (1)] [18,20,33] and rigorously justified [26,27] even though a local equilibrium does not exist. In quantum coherent conductors, the local temperature variations can be understood in terms of constructive and destructive interference of electron waves entering the probe from the two reservoirs [18,33]. For example, in Fig. 2, the cold (hot) spots correspond to a situation where the transmission of electron waves from the hot (cold) reservoir into the probe is suppressed. The effect is analogous to the cold spots arising in food heated by a coherent microwave source in a microwave oven. The wavelength of such quantum coherent temperature oscillations in graphene is related to that of the Friedel oscillations [20] and may be tuned by appropriate gating [36]. It is possible to have dramatic temperature variations within a single bond length, as seen in the central hexagon in Fig. 3 (see also Ref. [18]), and our method is capable of mapping such subangstrom temperature variations. However, we reiterate that our method relies only upon the general applicability of the Wiedemann-Franz law (not on quantum coherence) and have explicitly shown in Appendix C that the Wiedemann-Franz law is valid when the transport is dominated by elastic scattering processes.

Figure 3 shows the variations in temperature for a voltage bias of  $V_{\text{blue}} - V_{\text{red}} = k_B T_0 / e$ , with  $T_0 = 4$  K, so that the transport is within the linear response regime. The gating for this case has been chosen to be  $\mu_0 = -2.58$  eV such that there is an enhanced thermoelectric effect. The tunneling currents from the thermoelectric circuit, under these gating conditions, are of the order of 100 pA with a maximum tunneling current of about  $I = 150$  pA and are resolvable under standard lock-in techniques. The variation of the contact temperature is taken to be  $\Delta T = (10\%) T_0$  with  $T_0 = 4$  K. The resolution of the tunneling current is an important point especially for the measurement of the thermoelectric response coefficient  $\mathcal{L}_{p\alpha}^{(1)}$  and has been covered in greater detail in Appendix E. The same temperature scale is used for both panels in Fig. 3 and there is excellent agreement between  $T_p^{(\text{exact})}$  and  $T_p^{(\text{WF})}$ . The temperature variations shown here are solely the result of the voltage bias and are given by the first term in Eq. (5). Under voltage bias, temperature variations arise due to Peltier cooling or heating in the system [32], as well as Joule heating. Joule heating is omitted in linear response theory, and is negligible at the bias of 0.34 mV shown in Fig. 3. Since the variations in Fig. 3 are purely due to the thermoelectric effect, the EA definition would have noted no temperature variations at all.

The disagreement between the exact solution and our method are due to higher-order contributions in the

Sommerfeld series, which are extremely small [cf. Eq. (6)]. An explicit expression for the first Sommerfeld correction in the WF law has been derived in Appendix C. The discrepancy between  $T_p^{(\text{WF})}$  and  $T_p^{(\text{exact})}$  defined by  $|T_p^{(\text{WF})} - T_p^{(\text{exact})}|/T_p^{(\text{exact})}$  is less than 0.01% for the temperature bias case in Fig. 2, whereas their discrepancy for the voltage bias case in Fig. 3 is less than 0.2%.

## VI. CONCLUSION

It has proven extraordinarily challenging to achieve high spatial resolution in thermal measurements. A key obstacle has been the fundamental difficulty in designing a thermal probe that exchanges heat with the system of interest but is thermally isolated from the environment. We propose circumventing this seemingly intractable problem by inferring thermal signals using purely electrical measurements. The basis of our approach is the Wiedemann-Franz law relating the thermal and electrical currents flowing between a probe and the system of interest.

We illustrate this alternative approach to nanoscale thermometry with simulations of a scanning tunneling probe of a model nanostructure consisting of a graphene flake under thermoelectric bias. We show that the local temperature inferred from a sequence of purely electrical measurements agrees exceptionally well with that of a hypothetical thermometer coupled locally to the system and isolated from the environment. Moreover, our method provides the *electronic* temperature decoupled from all other degrees of freedom and can therefore be a vital tool to characterize nonequilibrium device performance. Our proposed *scanning tunneling thermometer* exceeds the spatial resolution of current state-of-the-art thermometry by some 2 orders of magnitude.

## ACKNOWLEDGMENTS

The authors gratefully acknowledge useful discussions with Brian J. LeRoy and Oliver L.A. Monti. This work was supported by the U.S. Department of Energy (DOE), Office of Science, under Award No. DE-SC0006699.

## APPENDIX A: SYSTEM HAMILTONIAN

The  $\pi$ -electron system of graphene is described within the tight-binding model,  $H_{\text{gra}} = \sum_{\langle i,j \rangle} t_{ij} d_i^\dagger d_j + \text{H.c.}$ , with nearest-neighbor hopping matrix element  $t_{ij} = -2.7$  eV. The coupling of the system with the contact reservoirs is described by the tunneling-width matrices  $\Gamma^\alpha$ . We calculate the transport properties using nonequilibrium Green’s functions. The retarded Green’s function of the junction is given by  $G^r(\omega) = [\mathbb{S}\omega - H_{\text{gra}} - \Sigma_T(\omega)]^{-1}$ , where  $\Sigma_T = -i \sum_\alpha \Gamma^\alpha / 2$  is the tunneling self-energy. We take the contact-system couplings in the broad-band limit, i.e.,  $\Gamma_{nm}^\alpha(\omega) = \Gamma_{nm}^\alpha(\mu_0)$  where  $\mu_0$  is the Fermi energy of the metal leads. We also take the contact-system couplings

to be diagonal matrices  $\Gamma_{nm}^\alpha(\omega) = \sum_{l \in \alpha} \Gamma_\alpha \delta_{nl} \delta_{ml}$  coupled to  $\pi$  orbitals  $n, m$  of the graphene system. The nonzero elements of  $\Gamma^\alpha$  ( $\alpha = \{\text{blue, red}\}$ ) are at sites indicated by either a blue or red square in Figs. 2 and 3, corresponding to the carbon atoms of graphene covalently bonded to the contact reservoirs. The tunneling matrix element at each coupling site is set as  $\Gamma_\alpha = 0.5$  eV for both the contacts (blue and red).  $\mathbb{S}$  is the overlap matrix between the atomic orbitals on different sites and we take  $\mathbb{S} = \mathbb{I}$ , i.e., an orthonormal set of atomic orbitals. The tunneling-width matrix  $\Gamma^p$  describing the probe-sample coupling is also treated in the broad-band limit. The probe is in the tunneling regime and the probe-system coupling is weak (few meV) in comparison to the system-reservoir couplings.

## APPENDIX B: PROBE-SAMPLE COUPLING

The scanning tunneling thermometer is modeled as an atomically sharp Pt tip operating in the tunneling regime at a height of 3 Å above the plane of the carbon nuclei in graphene. The probe tunneling-width matrices may be described in general as [37]  $\Gamma_{nm}^p(\omega) = 2\pi \sum_{l \in \{s,p,d,\dots\}} C_l V_l^m V_l^{n*} \rho_l^p(\omega)$ , where  $\rho_l^p(\omega)$  is the local density of states of the apex atom in the probe electrode and  $V_l^m, V_l^n$  are the tunneling matrix elements between the  $l$  orbital of the apex atom in the probe and the  $m$ th,  $n$ th  $\pi$  orbitals in graphene. The constants  $C_l = C \forall l$  and has been determined by matching with the peak of the experimental conductance histogram [38]. We consider the Pt tip to be dominated by the  $d$ -orbital character (80%) although other contributions ( $s - 10\%$  and  $p - 10\%$ ) are also taken as described in Ref. [37]. In the calculation of the tunneling matrix elements, the  $\pi$  orbitals of graphene are taken to be hydrogenic  $2p_z$  orbitals with an effective nuclear charge  $Z = 3.22$  [39]. The tunneling-width matrix  $\Gamma^p$  describing the probe-system coupling is in general nondiagonal.

## APPENDIX C: ELASTIC TRANSPORT

We explicitly show the derivation of the Wiedemann-Franz law for elastic transport below. The steady-state currents flowing into reservoir  $p$ , through a quantum conductor where elastic processes dominate the transport, can be written in a form analogous to the multiterminal Büttiker formula [33]

$$I_p^{(\nu)} = \frac{1}{h} \sum_\alpha \int_{-\infty}^{\infty} d\omega (\omega - \mu_p)^\nu \mathcal{T}_{p\alpha}(\omega) [f_\alpha(\omega) - f_p(\omega)], \quad (\text{C1})$$

where

$$\mathcal{T}_{p\alpha}(\omega) = \text{Tr} \{ \Gamma^p(\omega) G^r(\omega) \Gamma^\alpha(\omega) G^a(\omega) \} \quad (\text{C2})$$

is the transmission function for an electron originating in reservoir  $\alpha$  to tunnel into reservoir  $p$ . Our notation uses

$\nu = 0$  to refer to the particle current and  $\nu = 1$  to refer to the electronic contribution to the heat current.  $G^r$  ( $G^a$ ) is the retarded (advanced) Green's function.  $\Gamma^p$  and  $\Gamma^\alpha$  are the tunneling-width matrices describing the coupling of the system to the probe and contact  $\alpha$ , respectively. However, in this paper, we like to express the measurement condition [Eq. (1)] in terms of the electrical current  $I_p$ , which is of course related to the particle current by

$$I_p = -eI_p^{(0)} = -\frac{e}{h} \sum_\alpha \int_{-\infty}^{\infty} d\omega \mathcal{T}_{p\alpha}(\omega) [f_\alpha(\omega) - f_p(\omega)], \quad (\text{C3})$$

whereas the electronic heat current is simply

$$J_p = I_p^{(1)}. \quad (\text{C4})$$

Operation within the linear response regime allows one to expand the Fermi functions  $f_\alpha$  and  $f_p$  to linear order near the equilibrium temperature and chemical potential

$$\begin{aligned} f_\alpha - f_p &= \left. \left( \frac{\partial f}{\partial \mu} \right) \right|_{\mu_0, T_0} (\mu_\alpha - \mu_p) + \left. \left( \frac{\partial f}{\partial T} \right) \right|_{\mu_0, T_0} (T_\alpha - T_p) \\ &= \left. \left( -\frac{\partial f}{\partial \omega} \right) \right|_{\mu_0, T_0} [-e(V_\alpha - V_p)] \\ &\quad + (\omega - \mu_0) \left. \left( -\frac{\partial f}{\partial \omega} \right) \right|_{\mu_0, T_0} \frac{(T_\alpha - T_p)}{T_0}. \end{aligned} \quad (\text{C5})$$

The electrical current

$$I_p = \sum_\alpha \mathcal{L}_{p\alpha}^{(0)} (V_\alpha - V_p) + \mathcal{L}_{p\alpha}^{(1)} \frac{(T_\alpha - T_p)}{T_0}, \quad (\text{C6})$$

to linear order in the voltage and temperature gradients. Using Eq. (C5) in Eq. (C1), we obtain the expressions for the linear response coefficients

$$\mathcal{L}_{p\alpha}^{(0)} = \frac{e^2}{h} \int_{-\infty}^{\infty} d\omega \mathcal{T}_{p\alpha}(\omega) \left. \left( -\frac{\partial f}{\partial \omega} \right) \right|_{\mu_0, T_0} \quad (\text{C7})$$

and

$$\mathcal{L}_{p\alpha}^{(1)} = \frac{-e}{h} \int_{-\infty}^{\infty} d\omega (\omega - \mu_0) \mathcal{T}_{p\alpha}(\omega) \left. \left( -\frac{\partial f}{\partial \omega} \right) \right|_{\mu_0, T_0}. \quad (\text{C8})$$

The heat current

$$J_p = \sum_\alpha \mathcal{L}_{p\alpha}^{(1)} (V_\alpha - V_p) + \mathcal{L}_{p\alpha}^{(2)} \frac{(T_\alpha - T_p)}{T_0}, \quad (\text{C9})$$

where we take  $\mu_p \approx \mu_0$  in Eq. (C1) since we are interested in terms up to the linear order. Again, we infer from Eqs.

(C5) and (C1) that

$$\mathcal{L}_{p\alpha}^{(2)} = \frac{1}{h} \int_{-\infty}^{\infty} d\omega (\omega - \mu_0)^2 \mathcal{T}_{p\alpha}(\omega) \left( -\frac{\partial f}{\partial \omega} \right) \Big|_{\mu_0, T_0}. \quad (\text{C10})$$

The derivative of the Fermi function appears in the expressions for all the linear response coefficients and we may use the Sommerfeld series expansion [28,33]. We find that

$$\begin{aligned} \frac{h}{e^2} \mathcal{L}_{p\alpha}^{(0)} &= \mathcal{T}_{p\alpha}(\mu_0) + 2\Theta(2)(k_B T_0)^2 \mathcal{T}_{p\alpha}^{(2)}(\mu_0) \\ &+ 2\Theta(4)(k_B T_0)^4 \mathcal{T}_{p\alpha}^{(4)}(\mu_0) + \dots \end{aligned} \quad (\text{C11})$$

and

$$\begin{aligned} -\frac{h}{e} \mathcal{L}_{p\alpha}^{(1)} &= 4\Theta(2)(k_B T_0)^2 \mathcal{T}_{p\alpha}^{(1)}(\mu_0) + 8\Theta(4)(k_B T_0)^4 \\ &\times \mathcal{T}_{p\alpha}^{(3)}(\mu_0) + 12\Theta(6)(k_B T_0)^6 \mathcal{T}_{p\alpha}^{(5)}(\mu_0) + \dots \end{aligned} \quad (\text{C12})$$

and

$$\begin{aligned} h\mathcal{L}_{p\alpha}^{(2)} &= 4\Theta(2)(k_B T_0)^2 \mathcal{T}_{p\alpha}(\mu_0) + 24\Theta(4)(k_B T_0)^4 \mathcal{T}_{p\alpha}^{(2)}(\mu_0) \\ &+ 60\Theta(6)(k_B T_0)^6 \mathcal{T}_{p\alpha}^{(4)}(\mu_0) + \dots, \end{aligned} \quad (\text{C13})$$

where we use the notation from Ref. [33]:  $\mathcal{T}_{p\alpha}^{(k)}(\mu_0)$  denotes the  $k$ th derivative of the transmission function  $\mathcal{T}_{p\alpha}(\omega)$  at  $\omega = \mu_0$  and  $\Theta$  is a numerical factor related to the Riemann-Zeta function

$$\Theta(k+1) = \left(1 - \frac{1}{2^k}\right) \zeta(k+1). \quad (\text{C14})$$

Explicitly,

$$\begin{aligned} \Theta(2) &= \frac{\pi^2}{12}, \\ \Theta(4) &= \left(\frac{7}{8}\right) \frac{\pi^4}{90}, \\ \Theta(6) &= \left(\frac{31}{32}\right) \frac{\pi^6}{945}. \end{aligned} \quad (\text{C15})$$

The transmission function has appreciable changes on an energy scale determined by the system's Hamiltonian and its couplings to the contacts. We thus define the characteristic energy scale  $\Delta$

$$\mathcal{T}_{p\alpha}(\mu_0) = \Delta^2 \mathcal{T}_{p\alpha}^{(2)}(\mu_0), \quad (\text{C16})$$

which is typically much larger than the thermal energy  $k_B T_0$  for most experimental setups.

The following relation connecting  $\mathcal{L}_{p\alpha}^{(0)}$  and  $\mathcal{L}_{p\alpha}^{(2)}$ , from Eqs. (C11) and (C13), is the Wiedemann-Franz law:

$$\mathcal{L}_{p\alpha}^{(2)} = \frac{\pi^2 k_B^2 T_0^2}{3e^2} \mathcal{L}_{p\alpha}^{(0)} \left[ 1 + \frac{8\pi^2}{15} \left( \frac{k_B T_0}{\Delta} \right)^2 + \dots \right]. \quad (\text{C17})$$

#### APPENDIX D: CALIBRATION OF TEMPERATURE

The thermoelectric circuit requires the calibration of the contact temperatures, which we describe here. The Pt heater is fabricated atop an electrically insulating layer above the metal contact  $\alpha$  and has a thermal conductivity  $\kappa_{hc}$  with the contact. The temperature of the Pt heater is inferred from its resistivity. The contact  $\alpha$  is heated when an electrical current is passed in the Pt heater but it also loses heat to the ambient environment, which is at the equilibrium temperature  $T_{\text{env}} = T_0$ . We denote the thermal conductivity between the contact and the ambient environment by  $\kappa_0$ . The thermal circuit is shown in Fig. 4.

The heat current flowing into the contact is given by

$$\dot{Q}_{\text{in}} = \kappa_{hc} (T_{\text{heater}} - T_{\text{contact}}) \quad (\text{D1})$$

whereas the heat current flowing out

$$\dot{Q}_{\text{out}} = \kappa_0 (T_{\text{contact}} - T_{\text{env}}). \quad (\text{D2})$$

In steady state, the rate of heat flow into the contact is equal to the rate of heat lost to the ambient environment and we

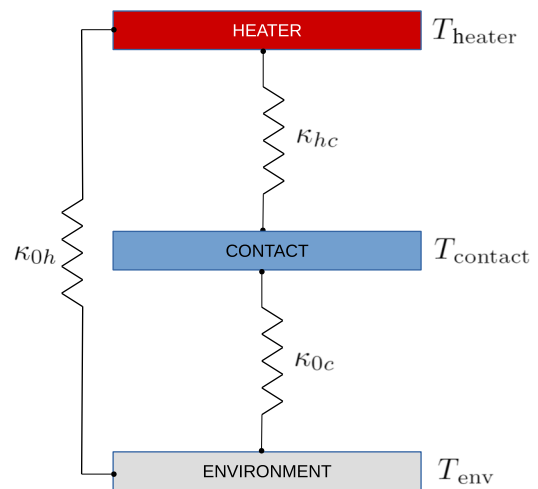


FIG. 4. Thermal circuit for heat transfer between the Pt heater, the metal contact, and the ambient environment. The contact temperature is nearly equal to that of the Pt heater,  $T_{\text{contact}} \approx T_{\text{heater}}$ , when they are in good thermal contact  $\kappa_{hc} \gg \kappa_0c$ .



find

$$T_{\text{contact}} = \frac{\kappa_{hc} T_{\text{heater}} + \kappa_{0c} T_{\text{env}}}{\kappa_{hc} + \kappa_{0c}}. \quad (\text{D3})$$

When the heater is in good thermal contact  $\kappa_{hc} \gg \kappa_{0c}$ , we find that

$$T_{\text{contact}} \approx T_{\text{heater}}. \quad (\text{D4})$$

An alternating voltage  $V(t) = V_{\text{max}} \cos(\omega t)$  results in a current  $I(t) = G_{\text{Pt}} V(t)$  in the heater. The power dissipated via Joule heating is given by

$$P = G_{\text{Pt}} V_{\text{max}}^2 \cos^2(\omega t) = \frac{1}{2} G_{\text{Pt}} V_{\text{max}}^2 [1 + \cos(2\omega t)], \quad (\text{D5})$$

which results in  $2\omega$  modulations of the heater temperature

$$T_{\text{heater}} = T_0 + \Delta T_{\text{max}} [1 + \cos(2\omega t)], \quad (\text{D6})$$

since the net power dissipated by the heater can be written as

$$P = \kappa (T_{\text{heater}} - T_0), \quad \text{where,} \quad (\text{D7})$$

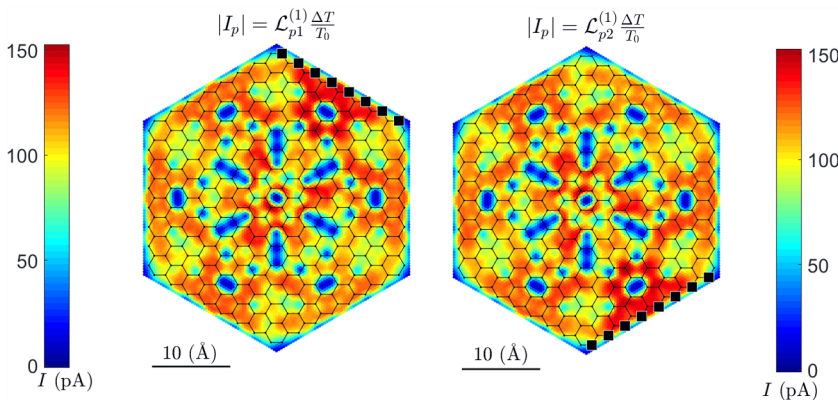
$$\kappa = \kappa_{0h} + \frac{\kappa_{hc} \kappa_{0c}}{\kappa_{hc} + \kappa_{0c}},$$

as seen from the thermal circuit shown in Fig. 4.

The temperature of the heater is inferred from the conductance (or resistivity) dependence of the Pt-heating element  $G_{\text{Pt}}(T)$ . The modulation frequency must be chosen so that  $\omega \ll 1/\tau$ , where  $\tau$  is the thermal time constant of the metal contact, so that it has enough time to thermally equilibrate. It is of course understood that such a frequency allows the heater itself to equilibrate and enter a steady state of heat transfer with the metal contact. The temperature modulations in the metal contact closely follow that of the heater when there is good thermal contact:

$$T_{\text{contact}}(t) = T_0 + \Delta T_{\text{max}} [1 + \cos(2\omega t)]. \quad (\text{D8})$$

We choose  $\Delta T_{\text{max}}$  such that the contact would reach a maximum temperature of  $T_0 + 2\Delta T_{\text{max}}$ . The calibration fixes  $\Delta T_{\text{max}}$  accurately.



We also note that the temperature modulations can be obtained by means other than using a Pt resistor. A graphene flake itself undergoes Joule heating and could therefore be used as a heating element so long as one is able to calibrate its temperature accurately.

## APPENDIX E: TUNNELING CURRENTS

### 1. Thermoelectric circuit

The tunneling current resulting from the heating of the contact is given by

$$I_p = \mathcal{L}_{p\alpha}^{(1)} \frac{(T_\alpha - T_0)}{T_0} \quad (\text{E1})$$

during the operation of the thermoelectric circuit. Standard lock-in techniques are employed to measure the current amplitude at frequency  $2\omega$ . It is easy to see from Eq. (D8) that the current amplitude

$$I_p|_{2\omega} = \mathcal{L}_{p\alpha}^{(1)} \frac{\Delta T_{\text{max}}}{T_0}. \quad (\text{E2})$$

We show the spatial variation of the tunneling current amplitude in Fig. 5. The probe is held at a constant height of  $3 \text{ \AA}$  above the plane of the sample. We assume a modest increase in the contact temperature by setting  $\Delta T_{\text{max}} = (10\%) T_0$  where the equilibrium temperature  $T_0 = 4 \text{ K}$ . The corresponding contact  $\alpha = \{1, 2\}$  is shown by black squares in Fig. 5 and represent the sites of the sample, which are covalently bonded to the metal contact  $\alpha$ .  $\alpha = 1$  is shown on the left panel and  $\alpha = 2$  is shown on the right panel in Fig. 5. The tunneling current amplitude is as high as  $150 \text{ pA}$  at some points on the sample and is therefore well within the reach of present experimental resolution. Since we illustrate our numerical results for an experiment performed at liquid He temperatures ( $4 \text{ K}$ ), the thermoelectric response is suppressed and gating becomes important. If, for example,  $T_0$  was set to  $40 \text{ K}$ , we would have a hundred-fold increase in the tunneling current amplitude [cf. Eqs. (E2) and (C12)] and gating would be less important.

FIG. 5. Amplitude of the tunneling current in the thermoelectric circuit. The left (right) panel shows the tunneling current amplitude resulting from the heating of the first (second) contact as shown with the black squares in the corresponding panel. The gating potential is set at  $\mu_0 = -2.58 \text{ eV}$  with respect to the Dirac point. The amplitude of temperature variations in the contacts [cf. Eq. (D8)] is taken to be  $10\%$  of the equilibrium temperature  $\Delta T_{\text{max}}/T_0 = 0.1$ .

### a. Gating

We find that the system has a sufficiently large thermoelectric response at 4 K, i.e., the current amplitude in Eq. (E2) is experimentally resolvable, when the system is gated appropriately. Indeed, our method works perfectly well for systems which do not have a good thermoelectric response. In such a case,  $\mathcal{L}_{p\alpha}^{(1)}$  would have a low value and would result in a current amplitude which is too small to measure. This merely implies that the thermoelectric contribution to the measured temperature is very small—that is, a voltage bias within the linear response regime does not lead to measurable differences in temperatures across the sample. We choose the system's gating so that the thermoelectric response is appreciable and there are measurable temperature differences across the sample even in the case of a voltage bias. We find this latter case more interesting.

The thermoelectric coefficient depends on the transmission derivative [cf. Eq. (C12)] near the equilibrium chemical potential. In Fig. 6, we show the transmission functions as a function of the chemical potential. The figure shows the transmission spectra into the probe from the two contacts  $\alpha = \{1, 2\}$  for one representative point on the sample where the probe is held at a height of 3 Å above the plane of the sample; the transmission spectra would change from point to point on the sample but will roughly resemble the one in Fig. 6. The contact  $\alpha = 1$  is shown in blue (dotted and dashed) whereas  $\alpha = 2$  is shown in red. We find that the transmission derivatives are enhanced when the chemical potential is tuned (via the gate voltage) to  $\mu_0 = -2.58$  eV and therefore illustrate the thermoelectric circuit for this choice of gating. The resulting temperature measurement is shown in Fig. 3 for a pure voltage bias. The spatial variations in the transmission derivatives would resemble the pattern shown in Fig. 5 [cf. Eq. (C12)].

## 2. Conductance circuit

The tunneling current resulting from the conductance circuit would simply be

$$I_p = \mathcal{L}_{p\alpha}^{(0)}(V_\alpha - V_p). \quad (\text{E3})$$

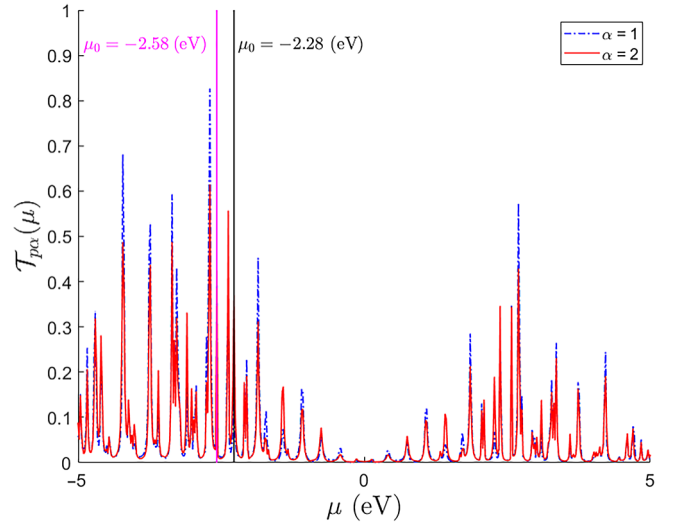
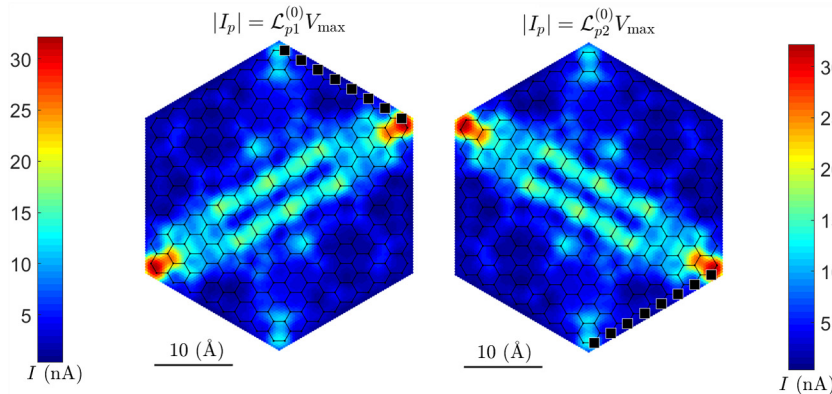


FIG. 6. Transmission function  $\mathcal{T}_{p\alpha}$  from contact  $\alpha$  into the STM probe  $p$ .  $\alpha = \{1, 2\}$  are shown in (dotted-dashed) blue and red, respectively. The conductance circuit measurement is illustrated at a gating potential of  $\mu_0 = -2.28$  eV (black vertical line). However, we illustrate the thermoelectric circuit at a gating potential of  $\mu_0 = -2.58$  eV (magenta vertical line) since the transmission functions show a large change at that choice of gating, thereby resulting in an enhanced thermoelectric effect.

We apply an ac voltage  $V_\alpha - V_p = V(t) = V_{\max} \cos(\omega t)$  across the contact-probe junction and measure the resulting tunneling current

$$I_p(t) = \mathcal{L}_{p\alpha}^{(0)} V_{\max} \cos(\omega t) \quad (\text{E4})$$

using standard lock-in techniques. The tunneling current amplitude at frequency  $\omega$

$$I_p|_\omega = \mathcal{L}_{p\alpha}^{(0)} V_{\max} \quad (\text{E5})$$

is measured across the sample as shown in Fig. 7. We set the amplitude of voltage modulations  $V_{\max} = 1$  mV and a scan of the sample is obtained by maintaining

FIG. 7. Amplitude of the tunneling current in the conductance circuit. The gating potential is set at  $\mu_0 = -2.28$  eV with respect to the Dirac point. The left (right) panel shows the tunneling current amplitude resulting from the voltage bias between the first (second) contact and the probe,  $V(t) = V_\alpha - V_p = V_{\max} \cos(\omega t)$ , as shown with the black squares in the corresponding panel.  $V_{\max} = 1$  mV.

the probe tip at a height of 3 Å above the plane of the sample. The tunneling current amplitude is as high as 30 nA for some regions in the sample. Generally, gating does not play as important a role in the measurement of conductances since we obtain tunneling currents of the order of a few nA for most choices of gating. The corresponding contact  $\alpha = \{1, 2\}$  is shown by black squares in Fig. 7 and represent the sites of the sample which are covalently bonded to the metal contact.  $\alpha = 1$  is shown on the left panel and  $\alpha = 2$  is shown on the right panel in Fig. 7. The resulting temperature measurement is shown in Fig. 2 for a pure temperature bias.

- 
- [1] Carlos D. S. Brites, Patricia P. Lima, Nuno J. O. Silva, Angel Millan, Vitor S. Amaral, Fernando Palacio, and Luis D. Carlos, Thermometry at the nanoscale, *Nanoscale* **4**, 4799 (2012).
- [2] G. Kucsko, P. C. Maurer, N. Y. Yao, M. Kubo, H. J. Noh, P. K. Lo, H. Park, and M. D. Lukin, Nanometre-scale thermometry in a living cell, *Nature* **500**, 54 (2013).
- [3] C. Yan Jin, Zhiyong Li, R. Stanley Williams, K.-Cheol Lee, and Inkyu Park, Localized temperature and chemical reaction control in nanoscale space by nanowire array, *Nano Lett.* **11**, 4818 (2011), pMID: 21967343.
- [4] Matthew Mecklenburg, William A. Hubbard, E. R. White, Rohan Dhall, Stephen B. Cronin, Shaul Aloni, and B. C. Regan, Nanoscale temperature mapping in operating microelectronic devices, *Science* **347**, 629 (2015).
- [5] J. S. Reparaz, E. Chavez-Angel, M. R. Wagner, B. Graczykowski, J. Gomis-Bresco, F. Alzina, and C. M. Sotomayor Torres, A novel contactless technique for thermal field mapping and thermal conductivity determination: Two-laser Raman thermometry, *Rev. Sci. Instrum.* **85**, 034901 (2014).
- [6] P. Neumann, I. Jakobi, F. Dolde, C. Burk, R. Reuter, G. Waldherr, J. Honert, T. Wolf, A. Brunner, J. H. Shim, D. Suter, H. Sumiya, J. Isoya, and J. Wrachtrup, High-precision nanoscale temperature sensing using single defects in diamond, *Nano Lett.* **13**, 2738 (2013), pMID: 23721106.
- [7] D. Teyssieux, L. Thiery, and B. Cretin, Near-infrared thermography using a charge-coupled device camera: Application to microsystems, *Rev. Sci. Instrum.* **78**, 034902 (2007).
- [8] Séverine Gomès, Ali Assy, and Pierre-Olivier Chapuis, Scanning thermal microscopy: A review, *Phys. Status Solidi (a)* **212**, 477 (2015).
- [9] P. Muralt and D. W. Pohl, Scanning tunneling potentiometry, *Appl. Phys. Lett.* **48**, 514 (1986).
- [10] B. G. Briner, R. M. Feenstra, T. P. Chin, and J. M. Woodall, Local transport properties of thin bismuth films studied by scanning tunneling potentiometry, *Phys. Rev. B* **54**, R5283 (1996).
- [11] Geetha Ramaswamy and A. K. Raychaudhuri, Field and potential around local scatterers in thin metal films studied by scanning tunneling potentiometry, *Appl. Phys. Lett.* **75**, 1982 (1999).
- [12] Weigang Wang, Ko Munakata, Michael Rozler, and Malcolm R. Beasley, Local Transport Measurements at Mesoscopic Length Scales Using Scanning Tunneling Potentiometry, *Phys. Rev. Lett.* **110**, 236802 (2013).
- [13] Kendal W. Clark, X.-G. Zhang, Gong Gu, Jewook Park, Guowei He, R. M. Feenstra, and An-Ping Li, Energy Gap Induced by Friedel Oscillations Manifested as Transport Asymmetry at Monolayer-Bilayer Graphene Boundaries, *Phys. Rev. X* **4**, 011021 (2014).
- [14] Philip Willke, Thomas Druga, Rainer G. Ulbrich, M. Alexander Schneider, and Martin Wenderoth, Spatial extent of a Landauer residual-resistivity dipole in graphene quantified by scanning tunnelling potentiometry, *Nat. Commun.* **6**, 6399 (2015).
- [15] R. Landauer, Spatial variation of currents and fields due to localized scatterers in metallic conduction, *IBM J. Res. Dev.* **1**, 223 (1957).
- [16] M. Büttiker, Chemical potential oscillations near a barrier in the presence of transport, *Phys. Rev. B* **40**, 3409 (1989).
- [17] Yonatan Dubi and Massimiliano Di Ventra, Thermoelectric effects in nanoscale junctions, *Nano Lett.* **9**, 97 (2009).
- [18] Justin P. Bergfield, Shauna M. Story, Robert C. Stafford, and Charles A. Stafford, Probing Maxwell's demon with a nanoscale thermometer, *ACS Nano* **7**, 4429 (2013).
- [19] J. Meair, J. P. Bergfield, C. A. Stafford, and Ph. Jacquod, Local temperature of out-of-equilibrium quantum electron systems, *Phys. Rev. B* **90**, 035407 (2014).
- [20] Justin P. Bergfield, Mark A. Ratner, Charles A. Stafford, and Massimiliano Di Ventra, Tunable quantum temperature oscillations in graphene nanostructures, *Phys. Rev. B* **91**, 125407 (2015).
- [21] C. C. Williams and H. K. Wickramasinghe, Scanning thermal profiler, *Appl. Phys. Lett.* **49**, 1587 (1986).
- [22] A. Majumdar, Scanning thermal microscopy, *Annu. Rev. Mater. Sci.* **29**, 505 (1999).
- [23] Fabian Menges, Heike Riel, Andreas Stemmer, and Bernd Gotsmann, Nanoscale thermometry by scanning thermal microscopy, *Rev. Sci. Instrum.* **87**, 074902 (2016).
- [24] Fabian Menges, Philipp Mensch, Heinz Schmid, Heike Riel, Andreas Stemmer, and Bernd Gotsmann, Temperature mapping of operating nanoscale devices by scanning probe thermometry, *Nat. Commun.* **7**, 10874 (2016).
- [25] J. Casas-Vázquez and D. Jou, Temperature in non-equilibrium states: A review of open problems and current proposals, *Rep. Prog. Phys.* **66**, 1937 (2003).
- [26] Charles A. Stafford, Local temperature of an interacting quantum system far from equilibrium, *Phys. Rev. B* **93**, 245403 (2016).
- [27] Abhay Shastry and Charles A. Stafford, Temperature and voltage measurement in quantum systems far from equilibrium, *Phys. Rev. B* **94**, 155433 (2016).
- [28] Neil W. Ashcroft and N. David Mermin, *Solid State Physics* (Holt, Rinehart and Winston, New York, 1976).
- [29] Nico Mosso, Ute Drechsler, Fabian Menges, Peter Nirmalraj, Siegfried Karg, Heike Riel, and Bernd Gotsmann, Heat transport through atomic contacts, *Nat. Nano* **12**, 430 (2017).
- [30] Longji Cui, Wonho Jeong, Sunghoon Hur, Manuel Matt, Jan C. Klöckner, Fabian Pauly, Peter Nielaba, Juan Carlos Cuevas, Edgar Meyhofer, and Pramod Reddy, Quantized

- thermal transport in single-atom junctions, *Science* **355**, 1192 (2017).
- [31] H.-L. Engquist and P. W. Anderson, Definition and measurement of the electrical and thermal resistances, *Phys. Rev. B* **24**, 1151 (1981).
- [32] Justin P. Bergfield and Charles A. Stafford, Thermoelectric corrections to quantum voltage measurement, *Phys. Rev. B* **90**, 235438 (2014).
- [33] Abhay Shastry and Charles A. Stafford, Cold spots in quantum systems far from equilibrium: Local entropies and temperatures near absolute zero, *Phys. Rev. B* **92**, 245417 (2015).
- [34] Jesse Crossno, Jing K. Shi, Ke Wang, Xiaomeng Liu, Achim Harzheim, Andrew Lucas, Subir Sachdev, Philip Kim, Takashi Taniguchi, Kenji Watanabe, Thomas A. Ohki, and Kin Chung Fong, Observation of the Dirac fluid and the breakdown of the Wiedemann-Franz law in graphene, *Science* **351**, 1058 (2016).
- [35] Makusu Tsutsui, Tomoji Kawai, and Masateru Taniguchi, Unsymmetrical hot electron heating in quasi-ballistic nanocontacts, *Sci. Rep.* **2**, 217 (2012).
- [36] Sosuke Inui, Charles A. Stafford, and Justin P. Bergfield, Emergence of Fourier's law of heat transport in quantum electron systems, *ACS Nano* **12**, 4304 (2018), pMID: 29648783.
- [37] Justin P. Bergfield, Joshua D. Barr, and Charles A. Stafford, Transmission eigenvalue distributions in highly conductive molecular junctions, *Beilstein J. Nanotechnol.* **3**, 40 (2012).
- [38] M. Kiguchi, O. Tal, S. Wohlthat, F. Pauly, M. Krieger, D. Djukic, J. C. Cuevas, and J. M. van Ruitenbeek, Highly Conductive Molecular Junctions Based on Direct Binding of Benzene to Platinum Electrodes, *Phys. Rev. Lett.* **101**, 046801 (2008).
- [39] J. D. Barr, C. A. Stafford, and J. P. Bergfield, Effective field theory of interacting  $\pi$  electrons, *Phys. Rev. B* **86**, 115403 (2012).